Structural, morphological, electrical, and magnetic characteristics of 20MnFe2O4-80SiO2 nanocomposite synthesized by the one-pot auto-combustion route.

Ali Salehizadeh (✉ ali.salehizadeh@dem.uc.pt)
University of Coimbra: Universidade de Coimbra

Benilde Costa
University of Coimbra Centre for Physics: Universidade de Coimbra Centro de Fisica

V. H. Rodrigues
University of Coimbra Centre for Physics: Universidade de Coimbra Centro de Fisica

Jean-Marc Greneche
Le Mans Université: Le Mans Universite

M.A. Valente
University of Aveiro: Universidade de Aveiro

Manuel Graça
University of Aveiro: Universidade de Aveiro

Structural, morphological, electrical, and magnetic characteristics of 20MnFe₂O₄-80SiO₂ nanocomposite synthesized by the one-pot auto-combustion route.

S.A. Salehizadeh[1*], B.F.O. Costa[2], V. H. Rodrigues[2], J-M. Greneche[3], M.A. Valente[4] and M.P.F. Graça[4].

[1]SEG-CEMMPRE, Mechanical Engineering Department, University of Coimbra, 3030-788 Coimbra, Portugal.

[2]CFisUC, Physics Department, University of Coimbra, 3004-516 Coimbra, Portugal.

[3]Institut des Molécules et Matériaux du Mans IMMM UMR CNRS 6283, Le Mans Université, Avenue Olivier Messiaen, F-72085 Le Mans, France.

[4]i3N - Department of Physics, University of Aveiro, 3810-193, Aveiro, Portugal.

[*]Corresponding author: ali.salehizadeh@dem.uc.pt

Abstract

We report an investigation of the structural, morphological, the ac-dc electrical, magnetic, and Mössbauer spectroscopy properties of 20MnFe₂O₄-80SiO₂ nanocomposite prepared using a one-step and facile auto-combustion approach. XRD pattern shows the formation of MnFe₂O₄ nanocrystallite without any crystallization of the SiO₂ phase. However, the presence of a secondary phase of the nanosized α-Fe₂O₃ particles was also detected. The morphological analysis showed aggregation of polygonal magnetic nano-crystallites dispersed non-uniformly in a silica matrix.

The dc electrical measurements performed on a wide range of temperatures from 120 to 400 K showed the semiconducting nature of the nanocomposite. The temperature dependence of dc conductivity could be perfectly fitted to the nearest neighborhood hopping model with activation energy, ΔE_{NNH}, of 0.45 eV.

The Nyquist plots demonstrated a nonmonotonous thermally activated trend and non-Debye relaxation behavior. An equivalent circuit was successfully fitted to the complex impedance spectra. The variation of both grain and grain boundary conductivities as a function of temperature exhibited three distinct regions, semiconducting-metallic-semiconducting with different activation energies over the measured temperature window. The provided description of such behavior is further advocated by the ac conductivity and dielectric modulus studies.

VSM measurements revealed that the nanocomposite magnetic behavior deviates from the ideal non-interacting superparamagnetic picture, due to the presence of α-Fe₂O₃ nanocrystalline impurities and relatively intensive exchange interactions between ions.

Mössbauer spectra showed the presence of Fe^{3+} ions with sixfold environment and also confirmed the existence of a sextet related to α-Fe_2O_3 with a quantity of 28% out of magnetic components. Fe^{3+} superparamagnetic doublets were also found within the fitting procedure.

1) **Introduction**

Nanostructured spinel ferrites including manganese ferrite have been vastly studied in recent years because of their superior magnetic, catalytic, chemical stability, and electrical conductivity properties [1, 2]. Manganese ferrite nanoparticles (MnFe NPs) have shown a high value of the magnetic susceptibility when compared to other ferrite nanoparticles, high chemical stability, easy synthesis process, high resistivity, soft magnetic behavior, and intermediate saturation magnetization [3, 4]. These unique characteristics of MnFe NPs have brought potential merits for them to be utilized in several technological applications including MRI [4], targeted drug delivery [5], microwave, inductance, magnetic recording media, electronic devices, and magnetic storage devices, [6] and gas sensors [7].

The structural characteristics of face-centered cubic (FCC) inverse spinel manganese ferrite have been extensively investigated [9-12]. The studies have shown that several parameters such as the particle, size, synthesis method, doping state, and the cations distribution in spinel structure sublattices can tune the electrical and magnetic properties of the ferrite nanocrystals [13, 14]. It was demonstrated that to improve the functionality of the ferrite nanocrystallites and enhance their efficiency in technological and industrial applications, a common approach is the dispersion of magnetic nanoparticles in inert organic/inorganic matrices like polymers, amorphous silica, in other words, fabrication of magnetic-silica (or polymeric) nanocomposites [15]. The addition of an amorphous silica matrix to the magnetic nanoparticles can result in a decrease in the net magnetization of the composition. The silica coating can also lead to the modulation of the cations arrangement, interparticle interactions, and surface/volume ratio of the magnetic nanoparticles, which changes the magnetic response of the nanocomposite [14, 15].

On the other hand, the electrical properties of magnetic-silica nanocomposites are determined by the molar ratio of each component, the degree of dispersion, and the interaction between the components [13]. It has been previously shown that the insulator/conductor transition observed in composites can be attributed to the temperature and frequency dependence of electrical parameters such as resistance and dielectric behaviors of grains and grain boundaries within the nanocomposite microstructure [13, 15].

By far, there have been numerous techniques to construct magnetic ferrite nanocomposites for example Stober sol-gel process [16], co-precipitation [17], microemulsion [18], hydrothermal [19], and auto combustion [20]. Sol-gel auto-combustion is to found be a more facile and time-saving and economically-efficient method than other wet-chemistry routes and the nanocomposites prepared by this method are compositionally stoichiometric, homogeneous with controlled microstructure [21]. Previously we have synthesized manganese ferrite-silica (MnFe/Si) nanocomposites using a sol-gel auto combustion route [22]. It was observed that for the stoichiometric MnFe/Si nanocomposites consisting of ≥20% (in mole) of magnetic

component (manages ferrite), crystallization of the secondary phase of nanosized hematite particles will occur. The aim of the present work is not to investigate the phenomenological reason for the formation of this secondary phase of hematite but to study its impacts on the structure, dc and ac conduction mechanism, and magnetic characteristics of $20MnFe_2O_4$-$80SiO_2$ nanocomposite. To the best of our knowledge, there is no report in which the influence of the formation of secondary phase of nanosized α-Fe_2O_3 particles on the temperature dependence of dc-ac conduction mechanism, cation distribution, and magnetic characterization of the nanocomposite has been comprehensively studied. Therefore in this paper, various characterization techniques, including XRD, Raman, TEM, dc-ac electrical measurements, VSM, and Mossbauer spectroscopy, were employed to logically correlate the conduction transport and the magnetic interactions occurring within the nanocomposite. Inclusively the anomalous ac-dc conductivity behavior and magnetic characteristics of the synthesized nanocomposite induced by the formation of the hematite structure as a function of temperature was investigated.

2) Experimental Procedure

To synthesize the $20MnFe_2O_4$-$80SiO_2$ nanocomposite, all raw materials, analytical grade iron nitrate (99% purity), manganese nitrate (≥97% purity), TEOS (≥ 98% in solution), ammonia (≈30% in solution) and citric acid (98% purity) were purchased from MERCK. An aqueous solution of metal nitrates (molar ratio of Fe: Mn=2:1) and citric acid (CA) with 1:1 molar ratio of metals to CA were prepared using the proper amount of the starting materials. The aqueous metal nitrates and the CA solutions were stirred for 0.5 h separately and then mixed together. Then, the metal nitrates-citrate solution was continuously stirred for 1 h to have a homogenous solution. During the stirring process of the metal-citrate solution, a small quantity of ammonia was added to maintain the solution pH value at 4. To prepare the silica precursor, TEOS, water, and ethanol were mixed with a ratio of 1/10/4, respectively, and then added up to the metal nitrates-citrate solution, in appropriate proportion to have a stoichiometric manganese ferrite-silica nanocomposite. The mixed solution was constantly stirred for 24 h in the air at a temperature of 100 ºC, till the water and ethanol contents were removed and the sol was transformed into a viscous gel. The xerogel was dried at 300 °C in a preheated oven and then the oven temperature increased gradually to 600 ºC in when the ignition occurred the loose powder in dark brown color was formed. As of now, the composition is noted 20MnFe/Si where 20 is the molar percentage of manganese ferrite.

The X-ray diffraction patterns (XRD) were collected at room temperature, RT, over a 2θ range of 15°–120° with 0.01° steps, 1s time exposition per step, using a 2θ-θ coupled-mode Bragg-Brentano geometry, in a Bruker D8 Advance diffractometer with a Cu tube operating at 40kV and 40mA. To detect $CuK\alpha$ radiation with $\lambda = 1.54056$ Å an N-filter with a Lynxeye silicon area detector was used. The Rietveld refinement was performed on the experimental XRD data using FullProf software. In this method, a Voigt approximation estimating both instrumental and physical (such as defects, dislocations, and internal stress) effects in the broadening of the peaks, was applied to study the XRD profile.

3

The morphological investigation was executed by the transmission electron microscopy (TEM) Tecnai G2 20 S-TWIN with an electron source of LaB6 emitter and accelerating voltage of 200 kV. For TEM measurements, a small quantity of 20MnFe/Si powder was dissolved in ethanol and the solution was ultrasonicated instantly. Some drops of the solution were deposited on the carbon-coated Cu grid (Agar scientific) and the TEM images were acquired from the as-dried solution.

Powder pellets with a thickness and diameter of 2 and 5 mm were compressed by the molding equipment and used for performing Raman and dc-ac electrical measurements. The Raman spectroscopy was carried out in a T64000 Jobin Yvon SPEX spectrometer, using an Ar laser (λ = 532 nm) as an excitation font in a back-scattering geometry, the spectrum was obtained between 200 and 900 cm^{-1} at RT.

The electrodes acquired for the electrical and dielectric measurements were applied by covering both sides of the flat pellet with silver paint. The dc electrical conductivity (σ_{dc}) was measured by the two probe method using a Keithley 617 programmable electrometer/source. Impedance spectroscopy measurements were performed in the frequency interval of 100 Hz to 1 MHz using an Agilent 4294A Network Analyzer in the C_p-R_p configuration. The dc electrical and impedance measurements were characterized in the temperature range between 120 K and 400 K.

dc magnetic measurements in zero-field cooling (ZFC)-field cooling (FC) modes and also M-B plots were carried out using a Lakeshore vibrating sample magnetometer (VSM). For the magnetization vs temperature curves in ZFC and FC modes applied field was 0.1 T (1000 Oe) and the temperature ranges from 5 to 300 K. The M (B) loops were collected at various temperatures between 5 and 300 K and under an applied magnetic field of 10 T.

Mössbauer spectra were recorded at room temperature (RT) and 77 K in a transmission geometry *WissEL* spectrometer, using a source of ^{57}Co in a Rh matrix with an activity of 30 mCi. The sample was in powder form and placed in a Perspex sample holder. The spectra were fitted by the least squares method, with a set of Lorentzian lines determined using the *NORMO*S program distributed by *WissEL GmbH*. Isomer shifts are given relative to α–Fe measured at RT.

3) Results and discussion

3-1) XRD analysis: induction of a compressive strain

Figure 1.a shows the XRD pattern of 20Mn/Fe sample measured at room temperature confirming the formation of the cubic spinel structure of $MnFe_2O_4$ in agreement with the JCPDS no. 04-016-8331. However, crystallization of the secondary phase of α-Fe_2O_3 in the

sample was also detected. Moreover, the broad and low-intense hump at observed 2θ~23º corresponds to the short-range correlations in the amorphous silica phase [19].
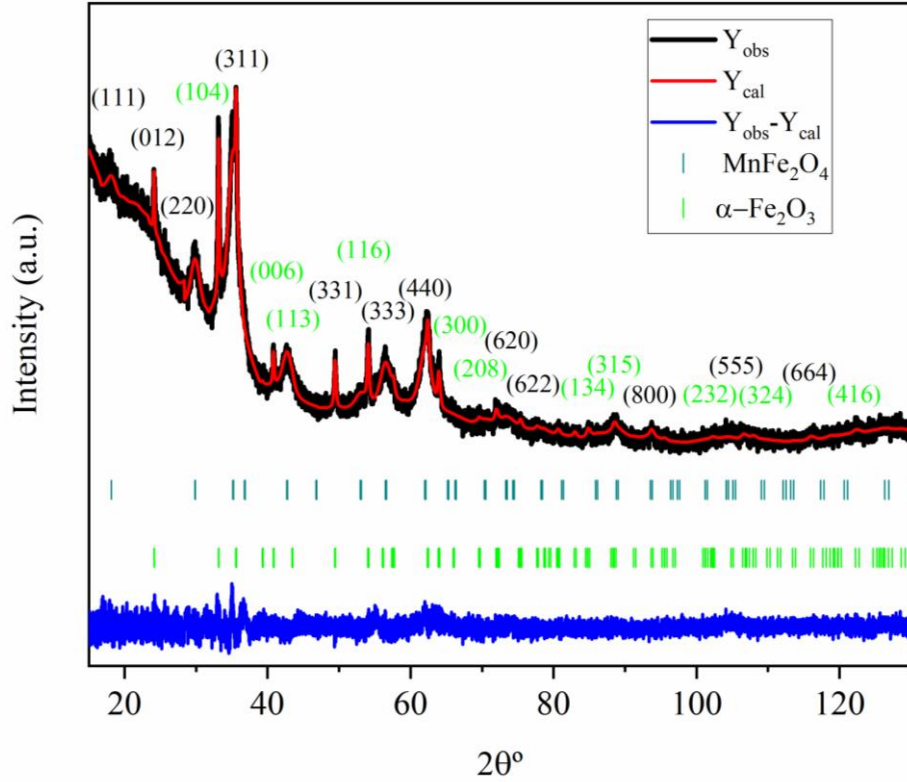

Figure 1) Rietveld refined XRD pattern of 20MnFe/Si

Based on the integral breadth method, the average particle size of nanoparticles, D_{Sch}, was determined using the Scherrer equation [20] :

$$D_{Sch}=\frac{K\lambda}{\beta.cos\theta} \tag{1}$$

Where K=0.94, λ is the wavelength of the X-ray beam, θ is the Bragg diffraction angle and β stands for the integral breadth. Considering the strain effect in the peak broadening, by means Stokes and Wilson (S-W) approach, one can calculate the apparent strain, η_{S-W}, as [20]:

$$\eta_{S-W}=\frac{\beta}{4tan\theta} \tag{2}$$

Williamson and Hall proposed a modified approach to study the XRD profile in which both size and strain contributions to the peak broadening are taken into account. From the Williamson-Hall (W-H) method, the total integral breath in reciprocal space ($\beta^*=\beta cos\theta/\lambda$) is denoted as [23]:

5

$$\beta^* = \frac{1}{D_{W-H}} + 2\varepsilon.d^* \qquad (3)$$

Where $d^* = 2\sin\theta/\lambda$ and D_{W-H} is the average crystallite size achieved from the W-H approach. By applying the W-H method to the data obtained from the Rietveld refinement and linearization of the W–H plot ($\beta\cos\theta$ vs. $4d\sin\theta$), we have calculated the average crystallite size and strain of the $MnFe_2O_4$ nanoparticles. The parameters deduced from the refinement and calculations regarding equations 1, 2, and 3, are enlisted in Table 1. As observed in figure 1, the complex background primarily comes from the huge contribution of internal strain, the defects due to the existence of amorphous silica and nanocrystalline α-Fe_2O_3 phases. Consequently, the de-convolution of XRD peaks is enfluenced by the proximity of coexisting hematite and manganese ferrite, and the peak broadening and the complexity of the polycrystalline composition affect the analysis of the refinement [19]. This is reflected in the high value of strain of η_{W-H} compared with η_{S-W} where both size and lattice strain is considered.

Table 1) Parameters extracted from the analysis of 20MnFe/Si. (the lattice parameter value, a; D_{W-H} and D_{Sch}; the strain values determined by W-H and S-W relations; and the activation energy of the nearest neighbor hopping (ΔE_{NNH}).

sample	a (Å)	D_{Sch} (nm)	$\eta_{S-W} \times (10^{-4})$	D_{W-H} (nm)	$\eta_{W-H} \times (10^{-4})$	ΔE_{NNH} (eV)
20MnFe/Si	8.46	7.2	75	6.5	313	0.45

In addition, it can be depicted that the average crystallite size (using both methods), of $MnFe_2O_4$ particles, was found close to 7 nm being much less than the value, 55 nm, determined for the reference sample, uncoated with silica, (not reported in this paper). Such reduction in crystalline size is due to the combined effect of the presence of α-Fe_2O_3 secondary phase and amorphous silica causing extra retarding force and strain which results in the lattice shrinkage. It is worth noting that we also could determine the average particle size of the α-Fe_2O_3 crystalline phase using the Scherrer approach; being 30 nm bigger than the one for the $MnFe_2O_4$ nanocrystalline phase. This observation further is supported by TEM analysis. Moreover, The content of hematite estimated from Rietveld refinement of X-ray diffraction data was found to be 24 % (in mol%) in agreement with the value deduced from Mössbauer spectrometry as later will be discussed.

3-2) Morphological studies and Raman spectroscopy

The morphological analysis of the synthesized nanocomposite was carried out through TEM study and the micrographs are shown in figures 2.a and b. As seen in the figure polygonal and oval particles formed loose aggregates and were randomly dispersed in an amorphous silica matrix. To determine the size and size distribution of the nanoparticles, at least 50 particles randomly selected from the TEM micrographs were considered. It was achieved that the particle size ranges from 4 to 32 nm and by applying a log-normal function to the size distribution histogram, the average particle size, D_{TEM}, was determined to be 7 nm in accordance with the XRD analysis. The selected

6

area electron diffraction (SAED) pattern (figure 2.a) supports, that the concentric rings characterize the amorphous nature of the silica matrix surrounding the bright small, and big spots corresponding to the nanocrystalline $MnFe_2O_4$ and Fe_2O_3 nanoparticles, respectively. Moreover, from the HRTEM image of 20MnFe/Si the parallel lattice fringes clearly exhibits the oriented aggregation of the $MnFe_2O_4$ and Fe_2O_3 nanocrystallites. Typically the lattice fringe of $d \approx 0.487$ nm agrees well with the separation between the (111) lattice planes of $MnFe_2O_4$ is brought in figure 2.b.
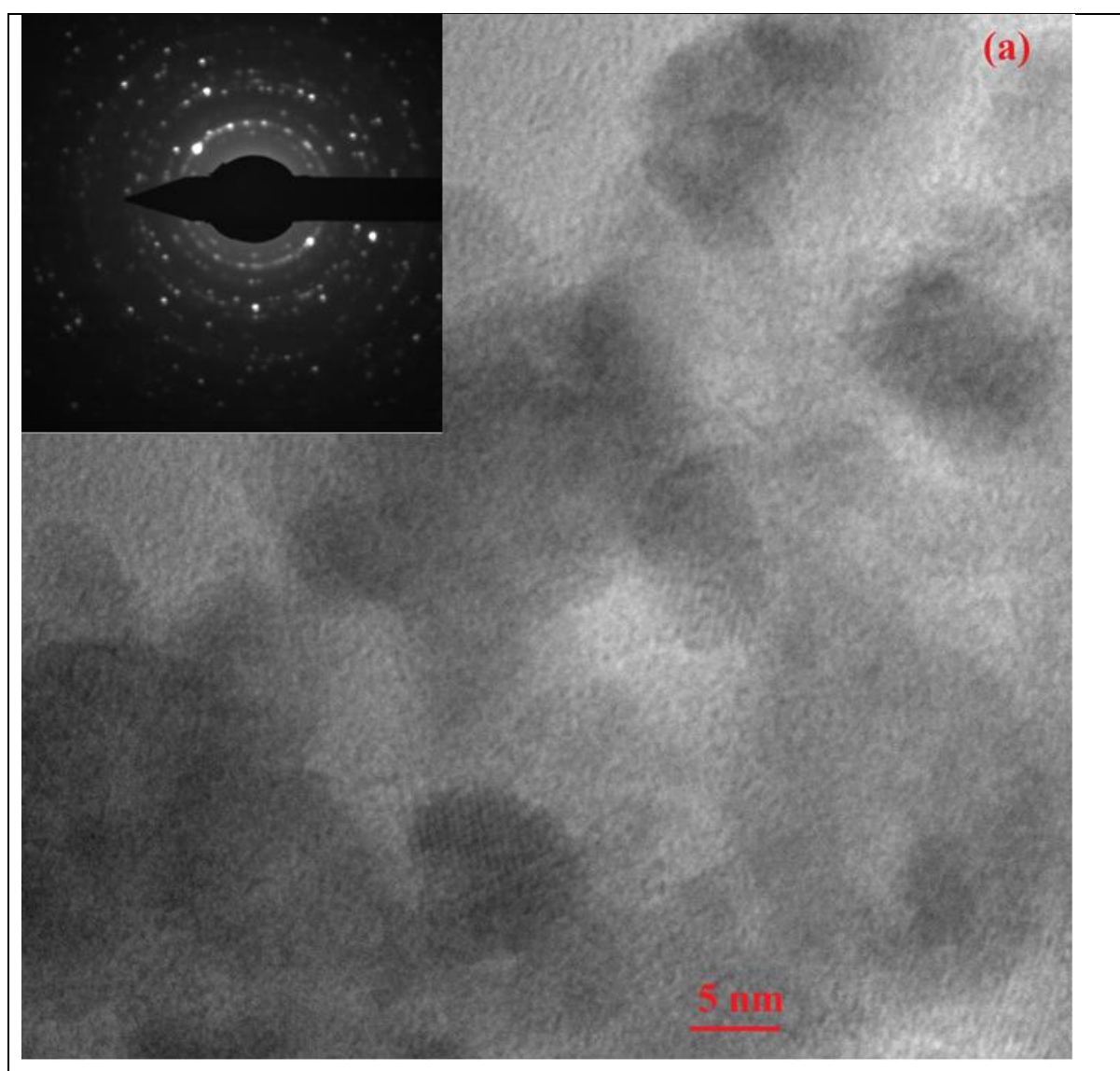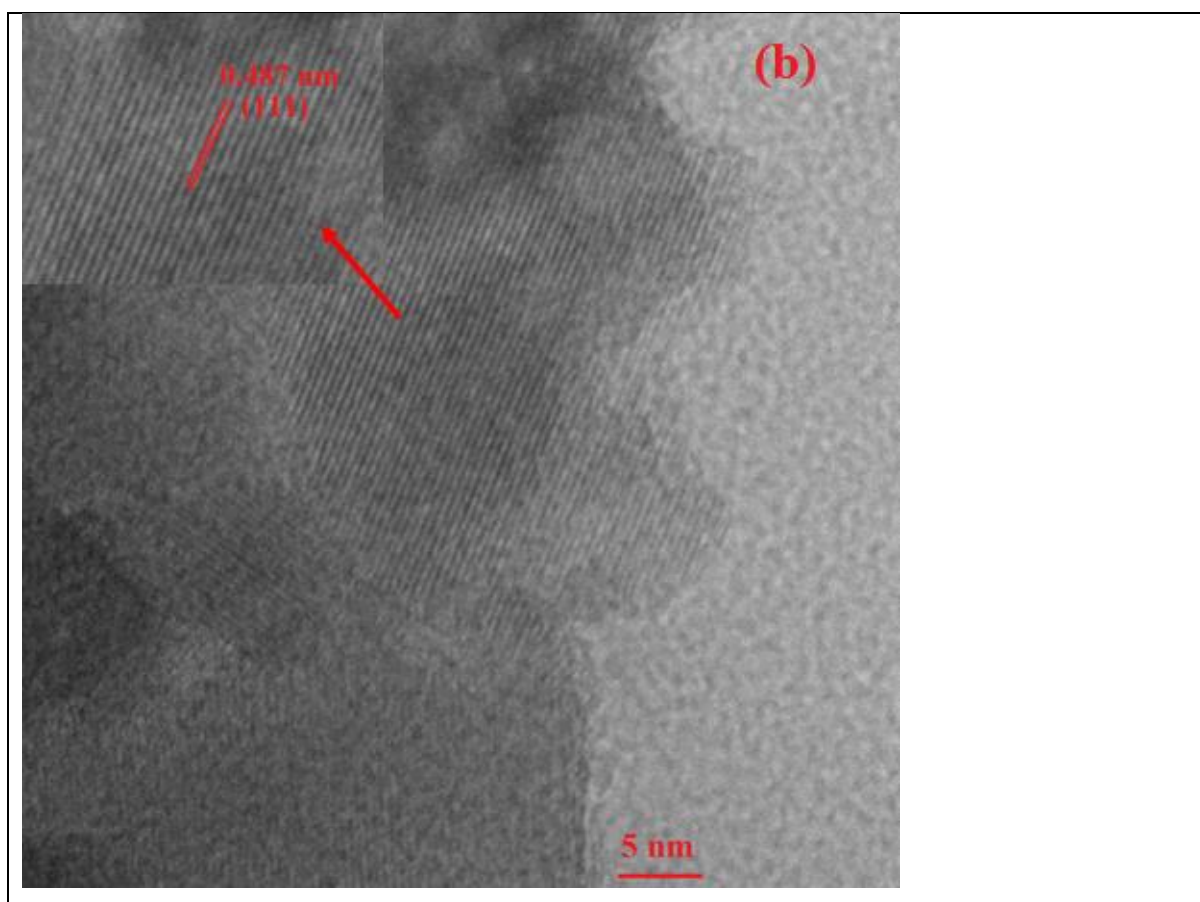
Figure 2.a) TEM image of 20MnFe/Si nanocomposite (the inset shows the corresponding SAED pattern) and b) Typical HRTEM image of 20MnFe/Si shows the lattice fringe related to (111) orientation of $MnFe_2O_4$.

Raman spectrum of 20MnFe/Si composition measured in the spectral region between 200 and 900 cm^{-1} at room temperature is represented in figure 3. First, the spectrum was baseline corrected in order to remove the background effect and then normalized with respect to the most intense peak in each spectrum. Identification of all possible vibration modes in the spectrum was obtained by deconvolution into individual Gaussian peaks as described precisely in [24] and labeled in alphabetic order as demonstrated in figure 3.
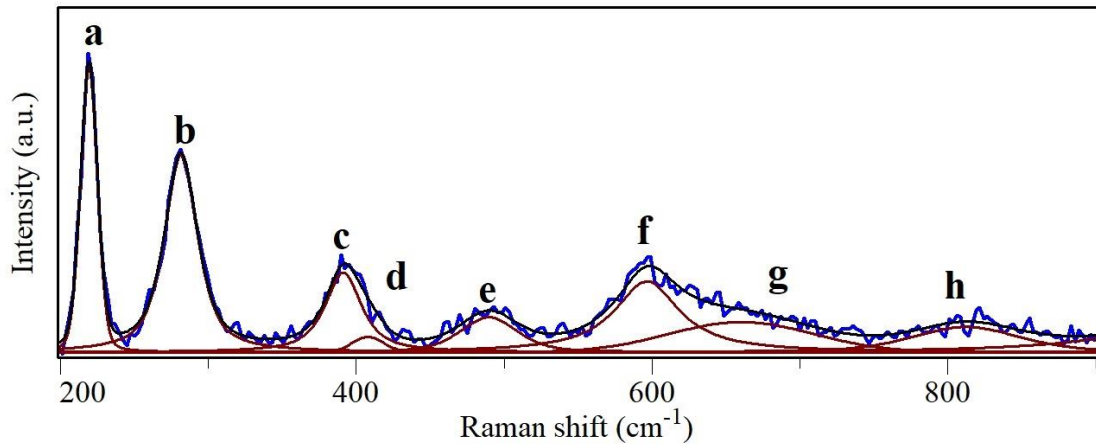
Figure 3) Raman spcetra of 20MnFe/Si nanocomposite recorded at RT.

The bands a and e detected at 218 and 594 cm^{-1} can be assigned to the A_{1g} and E_g modes, respectively, in hematite [25, 26]. Raman analysis reveals that four out of five first-order Raman active modes (A_{1g}, E_g, and $3T_{2g}$) characteristic of the cubic inverse-spinel structure O7h (Fd$\overline{3}$m) space group regarded to $MnFe_2O_4$ [7] could be observed. The A_{1g} appeared at 649 cm^{-1}, band f, is the symmetric stretch of tetrahedral FeO_4. The E_g at 393 cm^{-1} (band c) is regarded as symmetric bending of oxygen ions with respect to Fe. The T_{2g} (1) at 280 cm^{-1} is reflected in the translational motion of Fe–O in manganese ferrite. The peak at 393 cm^{-1} is caused by the anti-symmetric stretch of Fe and O assigned as T_{2g} (2) mode. The detection of T_{2g} (3), band d, at 489 cm^{-1} is due to an anti-symmetric bending of oxygen to Fe [27]. Raman feature at 810 cm^{-1} observed is regarded as the Si-O-Si stretching mode in the SiO_4 structure in amorphous silica [28].

The observed reduction in the number of allowed Raman bands of $MnFe_2O_4$ can be related to the particle size effect and loss of symmetry induced by the non-stoichiometric composition, the presence of vacancies, and lattice defects [29, 30] due to the formation of α-Fe_2O_3 secondary phase and the silica matrix inclusion in 20MnFe/Si. With decreasing in particle size and symmetry loss, the Raman peaks shift, the bands widen, and adjacent broad Raman peaks are overlapped, consequently, some permitted Raman modes cannot be detected. Similar behavior was already observed in nanosized $CoFe_2O_4$ particles [29].

9

3-3) dc and ac electrical investigations: an anomalous semiconducting-metallic-semiconducting transition

The dc electrical conductivity measurement as a function of temperature is illustrated in figure 4.a for 20MnFe/Si. The dc conductivity was determined using the following formula [31]:

$$\sigma_{dc} = \frac{t}{A.R} \tag{4}$$

Where t is the thickness of the pellet, A stands for the pellet area and R is the instantaneous resistance obtained from the dc conductivity measurement. The room temperature dc conductivity for 20MnFe/Si was achieved at 6.25×10^{-9} $(\Omega.m)^{-1}$ which is 3 orders less than the bare manganese ferrite nanoparticles prepared by the same method (not reported in this paper) being 1.56×10^{-6} $(\Omega.m)^{-1}$. In fact, SiO_2 amorphous sol-gel nanopowder has a low electrical conductivity (in the order of 10^{-12}- 10^{-15} $\Omega.m^{-1}$) due to its mesoporous conjugated network and high surface area [32]. Moreover, α-Fe_2O_3 nanocrystalline resistivity ranges from 10^{+6} to 10^{+9} $\Omega.m$ which is higher than $MnFe_2O_4$ nanoparticles [33]. Therefore adding insulting amorphous silica and formation of the secondary phase of hematite nanoparticles results in an abrupt reduction of conductivity in 20MnFe/Si compared with bare $MnFe_2O_4$ nanoparticles. The dc conductivity variation with a temperature of 20MnFe/Si exhibits the semiconducting behavior for 20MnFe/Si nanocomposite over the studied temperature range. Considering the insulating nature of silica, thus, it can be elucidated that the conduction mechanism is due to electron hopping conduction between Fe^{3+} to Fe^{2+} and Mn^{3+} to Mn^{2+}.

According to the nearest-neighbor-hopping (NNH) conduction model, the dc conductivity (σ_{dc}) in 20MnFe/Si nanocomposite can be stated by the Arrhenius equation yielding [34]:

$$\sigma_{dc} = \sigma_o \exp(-\Delta E_{NNH}/k_B T) \tag{5}$$

where σ_o is a constant, $k_B = 1.38 \times 10^{-23}$ $J.K^{-1}$ is the Boltzmann constant, and ΔE_{NNH} is defined as the activation energy of the nearest-neighbor hopping.

The ln σ_{dc} plot as a function of $1000.T^{-1}$ for the investigated sample is shown in figure 4. b. The ΔE_{NNH} value is obtained by linear fitting of the curve to eq. 5 and listed in table 1.
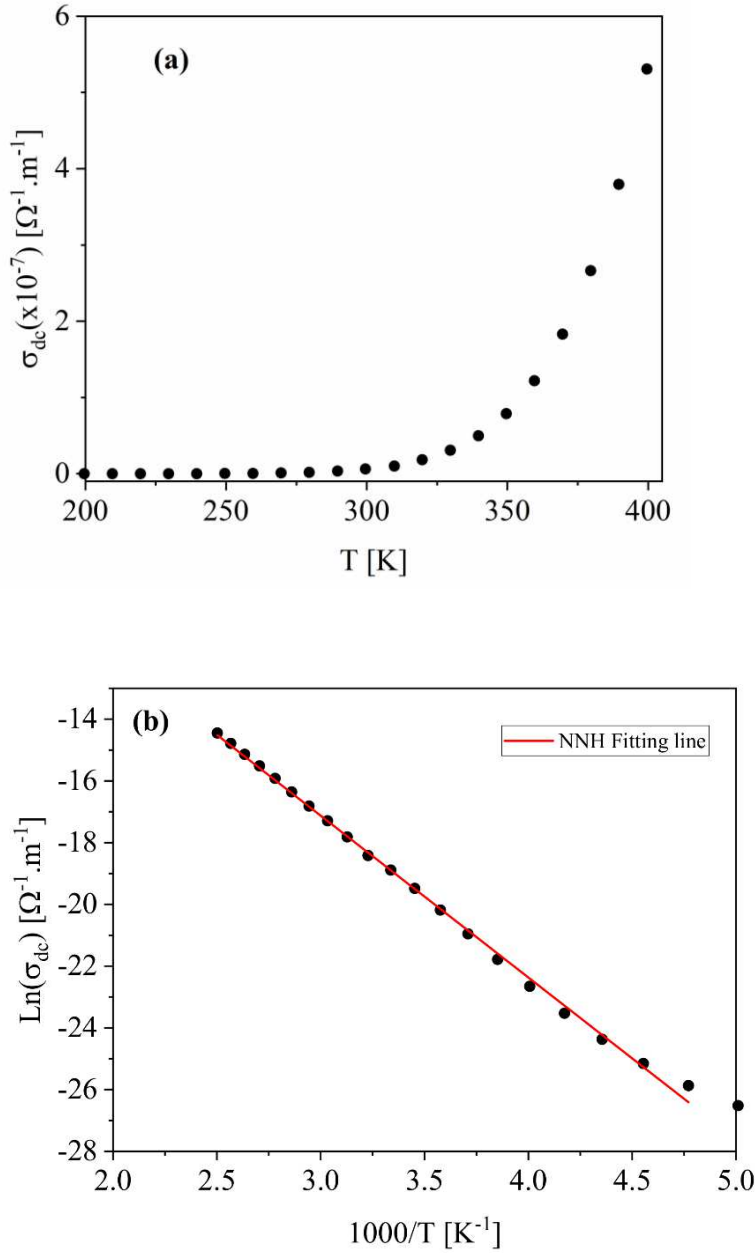
10

Figure 4.a) The dc conductivity as a function of temperature and b) the dependence of $Ln(\sigma_{dc})$ to the inverse of temperature, 1000/T.

Dielectric and ac conductivity measurements were performed over a frequency range of 10^2 Hz– 1 MHz and a temperature interval of 120 K to 400 K. The variation of the real part of the dielectric constant as a function of frequency and temperature at the selected temperatures and frequencies are given in figure 5 a and b, respectively.
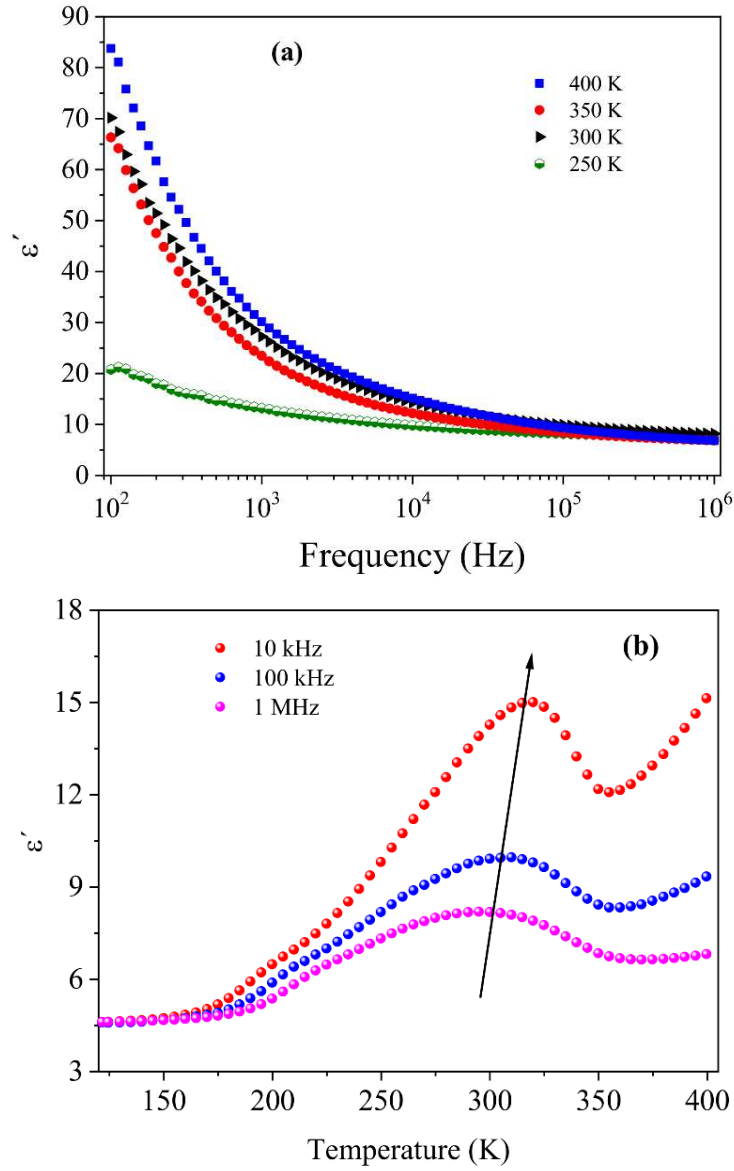
Figure 5 a and b) Variation of the real part of dielectric constant (ε´) with frequency and temperature, respectively.

According to figure 5.a, the dielectric constant monotonously reduces with frequency reaching a plateau at the high-frequency region between 10^5-10^6 Hz. Moreover, As observed in figure 5.b, the dielectric relaxation peak shifts to higher frequencies with temperature confirming the thermally active nature of the dielectric relaxation phenomena [35]. It is worth mentioning that the real part of the dielectric constant of bulk and nanosized SiO_2 is found be to 3.9 and 2.5 [36], respectively. While the dielectric constant for α-Fe_2O_3 nanoparticles ranges from 5 to 120

[37], dependent on the size and synthesis technique, being much less than the ones for manganese ferrite which varies from 10^2 to 10^5 as the size goes from nanoscale to the bulk scale [38]. According to the Mossbauer's studies (as will be discussed in the following), 20MnFe/Si constitutes 28% of nanosized hematite particles, therefore, the high value of the real part of the dielectric constant at the low-frequency region, mainly results from the contributions of α-Fe_2O_3 and $MnFe_2O_4$ nanoparticles. So it can be suggested that the electrons exchanging between Fe^{2+} and Fe^{3+} ions and the holes that transfer between Mn^{3+} and Mn^{2+} ions present in different sites are responsible for conduction and dielectric polarization. The dielectric behavior of 20MnFe/Si can be explained in terms of the Maxwell–Wagner theory of interfacial polarization [39]. In this model, the manganese ferrite-silica nanocomposite system is considered as a heterogeneous system composed of low resistive grains and high resistive grain boundaries. Based on this approach, the electrons and holes should pass through the conductive grains and the resistive grain boundaries. With a reduction in frequency, the electrons get in high resistance grain boundaries, and therefore the nanocomposite has a larger ε' value in the low-frequency range. In addition, the defects and oxygen vacancies accumulated in the grain boundaries act as active charge carrier traps leading to the form of an enhanced space charge polarization which leads to a higher dielectric constant in the low frequencies. As whilst, at higher frequencies, the alternation of the applied ac electric field hinders the electron/hole exchange consequently the polarization decreases [40].

Figure 6. a-b depicts the Nyquist plots (complex impedance spectra) of 20MnFe/Si composition measured at the selected temperatures. The impedance plots of 20MnFe/Si clearly show depressed single semi-circles suggesting the presence of a non-Debye type of relaxation in our composition with a relaxation time distribution due to the heterogeneous grain size and grain boundary effect [41]. Moreover, it is observed that the diameters of the semicircles decrease as the temperature increase from 250 K to 320 K, showing the semiconducting nature of the

13

samples with a negative temperature coefficient of resistance in this measured temperature range [42]. Although an anomalous trend can be detected in the temperature interval of 320 to 360 K, an increase in the semicircle diameter with the temperature characterizes a positive temperature coefficient of resistance, a feature of metallic behavior. With a further increase in temperature up to 400 K, the impedance spectra define a semiconducting kind of manner. To shed light on the unusual trend represented from the impedance spectra and correlate between the impedance spectra and the microstructure of the sample, we postulate an equivalent electrical circuit drawing.
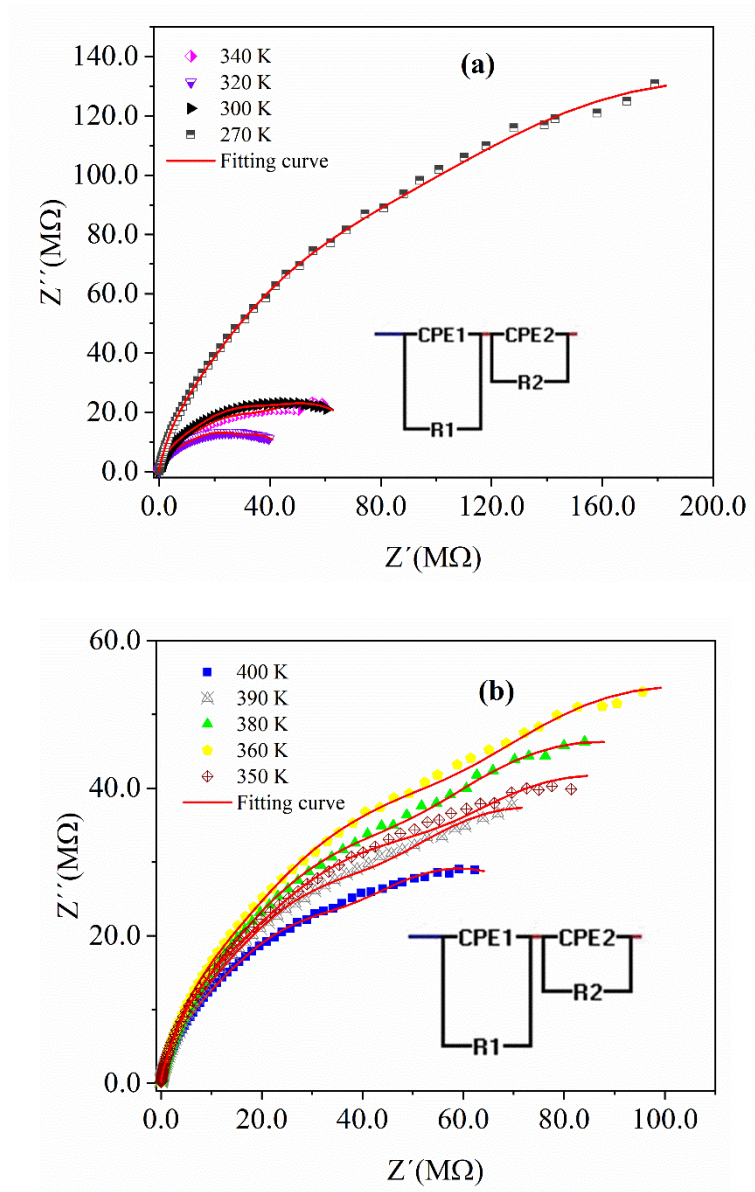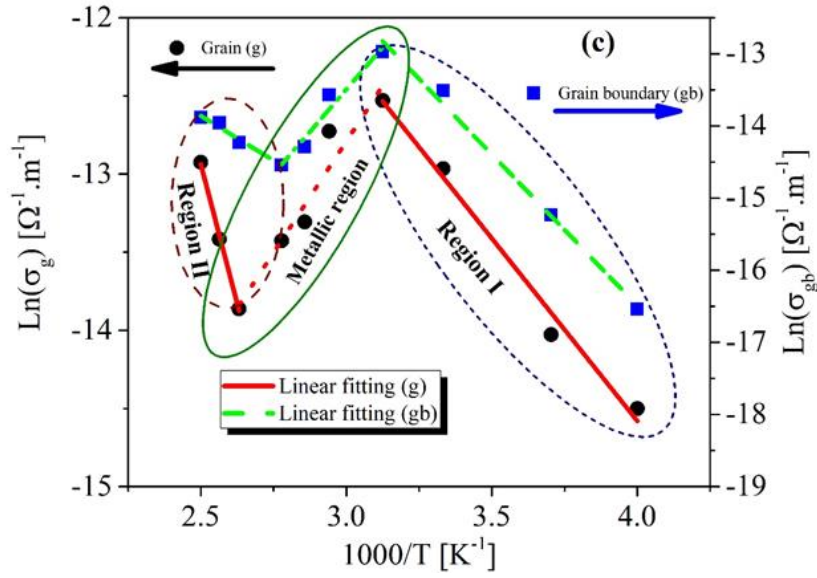
Figure 6.a and b) Complex impedance spectra at different temperatures (insets show the equivalent circuit proposed to fit the experimental spectra.). c) the NNH plots of the grain and grain boundary contributions in 20MnFe/Si. (the R^2=0.99)

The proposed equivalent circuit consists of a series combination $CPE_1\|R_1$ and $CPE_2\|R_2$ (CPE, R circuit element in a parallel configuration), each representing contribution of grain and grain boundary (the inset of figure 6.a and b). The constant phase element (CPE) in the circuit suggests an unideal Debye behavior [39]. The capacitance value of the CPE element is given by $C=Q^{1/n}R^{(1-n)/n}$ where the n value ranges from zero (indicating pure resistive behavior) to unity (for capacitative nature). As illustrated in figure 6.a and b, the equivalent circuit perfectly fits the experimental data.

From the fitted curves, the values of grain resistance (R_g), grain boundary resistance (R_{gb}), interior grain capacitance (C_g) and grain boundary capacitance (C_{gb}) were obtained and listed in table 2.

According to table 2, the R_g-R_{gb} and C_g-C_{gb} variations with temperature show $C_{gb}>C_g$ and $R_{gb}>R_g$ over the measured temperature window.

Table 2) The grain and grain boundary capacitance, C_g and C_{gb}, grain and grain boundary resistance, R_g and R_{gb}, values extracted from the fitting of the proposed equivalent circuit for 20MnFe/Si. (all values are with ±2% error)

20MnFe/Si				
Temperature	R_g	C_g	R_{gb}	C_{gb}
(K)	(MΩ)	(pF)	(MΩ)	(pF)
270	59.8	2.33	229	5.51
290	35	2.28	68.5	10.1
300	25.1	2.20	43.1	12.9
320	17.1	2.07	24.6	16.3
340	24.1	1.96	40.9	15.1
360	44.7	2.16	90.9	11.7
380	42.2	2.48	78.3	14.4
400	32.4	2.80	49.3	19.9

We also could obtain the grain and grain boundary conductivity, σ_g and σ_{gb}, using the following equation [43]:

$$\sigma_{g,gb}=L/(A.R_{g,gb}) \tag{6}$$

where A and L are the area and thickness of the sample, respectively.

The temperature variation of σ_g and σ_{gb} for all the samples are plotted in figure 6.c.

Based on the NNH model, for a wide temperature range, the temperature dependence of σ_g and σ_{gb} can be expressed by [43]:

$$\sigma_{g,gb}= \sigma_{g,gb(o)}.\exp(-\Delta E_{a(g,gb)}/k_BT) \tag{7}$$

Where $\Delta E_{a(g)}$ and $\Delta E_{a(gb)}$ are the activation energy of the grain and grain boundary, respectively. From the slopes of the linear fittings, we have calculated the values of $\Delta E_{a(g)}$ and $\Delta E_{a(gb)}$ for 20MnFe/Si which are listed in Table 3.

Figure 6.c indicates the $Ln(\sigma_g)$ and $Ln(\sigma_{gb})$ vs 1000/T plots for 20MnFe/Si. In the temperature range 250 to 320 K, referred to as region I, the observed reduction in the grain and grain boundary resistance is because of thermal activation of the localized charge carriers [39]. In manganese ferrites, conduction comes from the hopping of localized d electrons of transition metal ions residing in oxygen lattices. Due to the electrostatic interaction via superexchange paths Fe^{3+}-O-Fe^{3+} and Mn^{2+}-O-Mn^{2+}, the cation 3d level is divided into weak doubly degenerate

e_g levels and stable triply degenerate t_{2g} levels [44]. (As later will be discussed from the room temperature Mossbauer spectroscopy data, the iron ions present only Fe^{3+} valence state.) In region I, the density of hopping carriers within the grain decreases, due to the formation of the secondary phase of hematite and the absence of Fe^{2+} sites. Moreover, because of electronic entanglement and surface/core spin disorders, the energy of e_g electrons (E_k) is lower than that applied by the grain boundary and the charge carriers get trapped.

Goodenough's theory [45] has suggested the coexistence of both cation–cation, and cation–anion-cation interactions in transition-metal oxides (TMOs). Based on this theory, If the strong cation-anion-cation interactions overcome the weak cation-cation interactions, TMOs present semiconducting-insulating behavior. While, if the direct cation-cation interactions between octahedral B-site dominate, a transition from the semiconducting to the metallic behavior takes place with the temperature. Also, the presence of cations with bivalence states can lead to the metallic character below the Curie temperature as previously reported for nickel ferrite nanoparticles [44]. In the case of our study, $MnFe_2O_4$ is formulated as $(Fe^{3+})[Mn^{2+}Fe^{3+}]O_4^{2-}$ and the cation–anion-cation interactions between $[Fe^{3+}–O^{2-}–Fe^{3+}]$ and $[Mn^{2+}–O^{2-}–Mn^{2+}]$ are stronger than the cation–cation interaction causing a semiconducting behavior at the region below 320 K. According to Mossbauer spectra, due to the reduced value of the tetrahedral isomer shift compared to the octahedral isomer shift and the formation hematite secondary phase with the 6-folded Fe^{3+} ions, a fraction of Fe^{3+} ions are transferred to the six-fold (B) sites and reversely Mn^{2+} ions migrate to 4 coordinated A site. As the Fe^{3+} ions shift to the B sites the distance between the ions within the B site shortens and this induces an excessive strain, confirmed by the XRD study presented previously and agreed with the results from the $NiFe_2O_4$ nano-structured particles [46]. Resulting of the excessive strain, the surface exchange bonds may break, and a canted spin structure forms. The canted spins influence the $[Mn^{2+}–O^{2-}–Mn^{2+}]$ interactions and also weaken the AB-exchange interactions and as a consequence lower the magnetization value. Thus, it can be assumed that in the region below 320 K, the enhancement in the number of Fe^{3+} cations strengthens the exchange interaction between $[Fe^{3+}–O^{2-}–Fe^{3+}]$, and with an increase in temperature the probability of the charge carriers' delocalization between the $[Fe^{3+}–O^{2-}–Fe^{3+}]$ and $[Mn^{2+}–O^{2-}–Mn^{2+}]$ linkages promote and consequently the composition presents a semiconducting nature in this region.

However; beyond 320 K the tendency to oxidate/reduce Mn and Fe ions and create defects such as oxygen vacancies in the ferrite lattice may lead to the formation of Mn^{3+} and Fe^{2+} cations.

Resultantly, in this region from 320 to 360 K, the trapped states get delocalized, and the spins are aligned leading to creating effective conductive channels of [Fe^{3+}–Fe^{2+}] and [Mn^{2+}–Mn^{3+}] linkages. These channels delocalize the charge carriers and a transition from semiconducting behavior to metallic behavior occurs.

Above 360 K, due to the disordering of surface/core spins and also non-magnetic elements, the localized states reformed and the semiconducting feature reoccurs in region II, with different activation energy.

Figure 7.a shows the frequency dependence of the real part of ac conductivity in selected temperatures. The σ_{ac} variation with frequency can be divided into two regions: in the low-frequency region a plateau of conductivity while the conductivity is frequency dependent in the high-frequency region. The extrapolation of low-frequency σ_{ac} gives dc conductivity σ_{dc} which is attributed to the long-range translation motion of carriers.
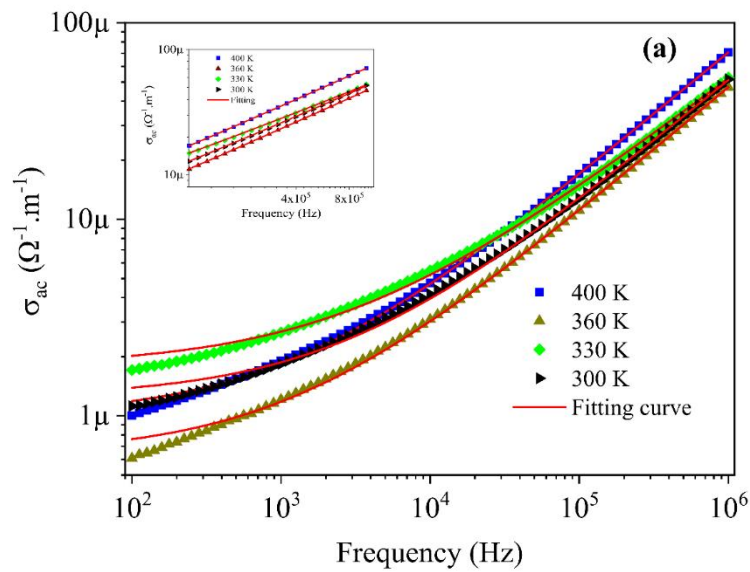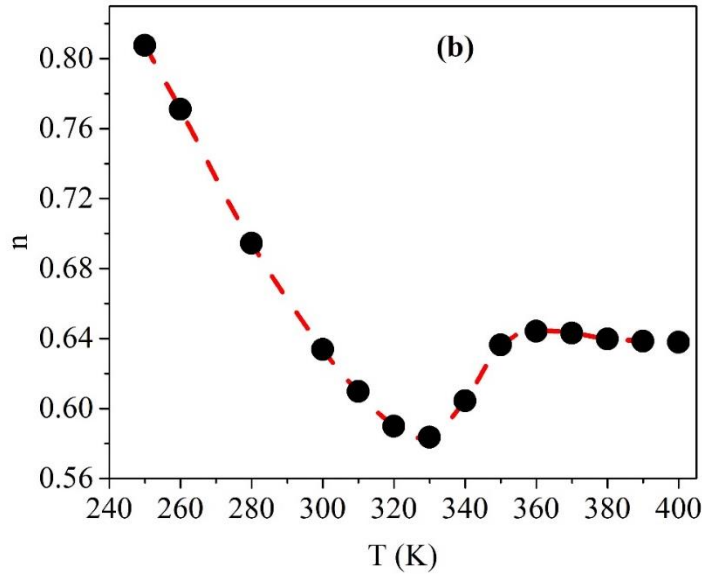
Figure 7.a) the ac conductivity vs. frequency plots measured at several temperatures and b) Variation of the universal exponent of n as a function of temperature. (the fitting´s R^2=0.99)

The conductivity frequency-dependent feature observed in 20MnFe/Si can be assigned to the relaxation phenomena taking place within the nanocomposite due to charge carriers hopping [39]. With increasing in temperature, the ac conductivity increases due to thermally generated charge carriers. Further, the ac conductivity follows the Johnscher's power law given by [35]:

$$\sigma_{ac}(\omega)= \sigma_{dc}+A\omega^n \tag{8}$$

where σ_{dc} is the dc conductivity, A is a constant which varies with temperature and indication of polarizability strength, ω is the angular frequency, and n ($0 \leq n \leq 1$) is an exponential factor that depends on both temperature and frequency and a scale of polaron interactions within nanocomposite structure.

The ac conductivity data were successfully fitted to Eq. 8 and the n values were obtained. Variation for universal exponent n as a function of temperature is shown in figure 7.b. Several models have been proposed based on the behavior of n such as QMT (Quantum tunneling mechanism, where the value of 'n' is independent of temperature), OLPT (Overlapping large polaron tunneling, where n reaches a minimum followed by increases with temperature), and CBH (Correlated barrier hopping, where n decreases with temperature) [41, 43, 44, 47].

According to figure 7.b, the exponent n strongly depends on the temperature for 20MnFe/Si. First, the value of n decreases with temperature and reaches to a minimum followed by an

19

increase in the value with further rising of the temperature up to 360 K. Above 360 K, the n is saturated and becomes constant. Therefore, in 20MnFe/Si below 360 K, the OLPT explain the conduction process while above 360 K the mechanism obeys the QMT model. In 20MnFe/Si composite, in the temperature interval of 260 K-360 K, due to the annihilation of Fe^{2+} valence state, the possibility of hopping charge pair, $Fe^{2+}-Fe^{3+}$, in this composite drops and the small non-overlapping polarons are not formed anymore. Therefore, in the case of a reduced number of hopping charges, the cations, Fe^{3+} and Mn^{2+}, surrounded by close-packed oxygen anions, O^{2-}, are isolated from each other, and, then the charge carrier is localized. This localization results in the creation of the polaron and the spatial extent of the polaron may broaden to several interatomic distances [43]. Hence, long-range Coulomb interaction occurs, and the neighboring sites' potentials superimpose on each other. Accordingly, the charge transport takes place via an overlapping large polaron tunneling process.

For temperatures above 360 K, the possible presence of multiple valence states of Mn and Fe ions ($Mn^{2+}-Mn^{3+}$ and $Fe^{2+}-Fe^{3+}$) and also Jahn–Teller distortion occurring in the composite creates defects the and the charge carrier may hop between site pairs over the potential barrier, the defect centers, separating them. Therefore, the correlated barrier hopping conduction mechanism is the dominant process in this temperature window [47].

To investigate the dielectric relaxation of the sample, the frequency dependence of the imaginary part of electrical modulus, M'', at different temperatures were plotted in figure 8.a. The plots show an asymmetric peak at each temperature indicating the spread of relaxation with a different time constant, and non-Debye behavior. Moreover, the variation of the relation with temperature presents a non-monotonous trend; first, the relation peak shifts toward to higher frequencies as the temperature increase from 260 to 320 K. From this point up to 360 K, region II, the relaxation peak shifts down to lower frequencies, again, in the temperature window of 360 to 400 K (region III), the relaxation peak shifts toward to higher frequencies with temperature. The relaxation time, τ, is defined as $\tau = \dfrac{1}{2\pi f_{max}}$ where f_{max} is the frequency in which the relaxation peak occurs [48]. The logarithmic representation of the relaxation time, $Ln(\tau)$, versus the inverse of temperature, 1000/T, is drawn in figure 8.b.
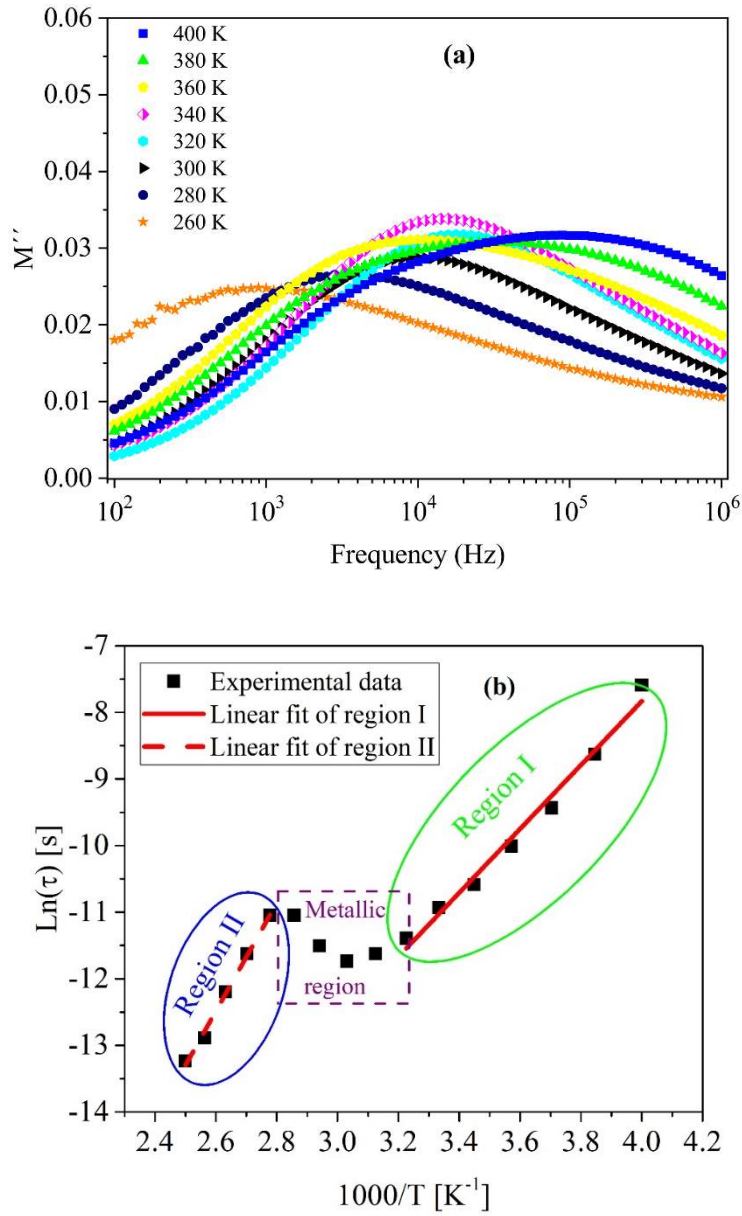
Figure 8.a) The modulus spectra measured at several temperatures b) the logarithmic representation of the relaxation time, Ln(τ), vs. the inverse of temperature, 1000/T.

The relaxation time as a function of temperature can be written in the form of the following Arrhenius equation and the dielectric modulus activation energy, $\Delta E_{M''}$, is extracted from the linearization of eq.6 to the experimnetal data and the obtained values are listed in table 3:

$$\tau_{M''} = \tau_o \cdot \exp(\Delta E_{M''}/k_B T) \tag{9}$$

Where τ_o is a constant parameter.

Table 3) The activation energy of the nearest neighbor hopping, ΔE_{NNH}; the activation energy of the grain (g) and grain boundary (gb), $\Delta E_{a(g,gb)}$; the dielectric modulus activation energy, $\Delta E_{M''}$. (all values are with ±0.1% error)

20MnFe/Si					
$\Delta E_{a(g)}$ (eV)		$\Delta E_{a(gb)}$ (eV)		$\Delta E_{M''}$ (eV)	
Region I	Region II	Region I	Region II	Region I	Region II
0.61	0.20	0.36	0.21	0.41	0.70

According to figure 8.b, three distinct regions can be identified which is clearly in resembling of the semiconducting→metallic→semiconducting transitions already observed in the impedance study.

In region I, the thermally activated $[Fe^{3+}–O^{2-}–Fe^{3+}]$ and $[Mn^{2+}–O^{2-}–Mn^{2+}]$ linkages are responsible for the relaxation and the charge carriers get more mobile as the temperature increases resulting in a shifting of the relaxation frequencies toward higher values. In region II, the shift of the relaxation peak toward a lower frequency supports our discussion of the delocalization of the charge carriers with the random distribution of the energy, and metallic behavior. With an increase in temperature, the lattice vibration increases, and some of the charge carriers scatter from the grain boundary planes [43]. The scattering reduces the mobility of the charge carriers and the metallic feature appears. Beyond 360 K, the localization sites are reproduced and the charge carriers get trapped again so the thermal agitation increases the charge carriers' mobility originating the semiconducting feature with different activation energy.

3-4) VSM and Mossbauer spectroscopy characterization: deviation from an ideal superparamagnetic picture

Figure 9.a presents the temperature dependence of the magnetization recorded at a B=100Oe and in ZFC/FC modes.

The ZFC curve shows a relaxation peak, T_b, characteristic for the superparamagnetic feature at 36 K and T_{irr}=257 K, the point where ZFC curve and FC curve separate from each other. The hysteresis curves measured at 5 and 300 K are given at figure 8.b.

Due to the lower thermal fluctuation of the magnetic moments, the magnetization at 5 K is clearly larger than that at 300 K.

As illustrated in figure 9.b, the hysteresis loops for 20MnFe/Si measured at 300 K do not saturate even for our highest field (B) (10 T). This indicates a magnetically hard component that can be associated with the surface spin disorder [49]. The observed behavior also might be addressed to the canting of spins in the ferrimagnetically ordered Mn-ferrite and hematite particles due to fairly strong superexchange interactions.
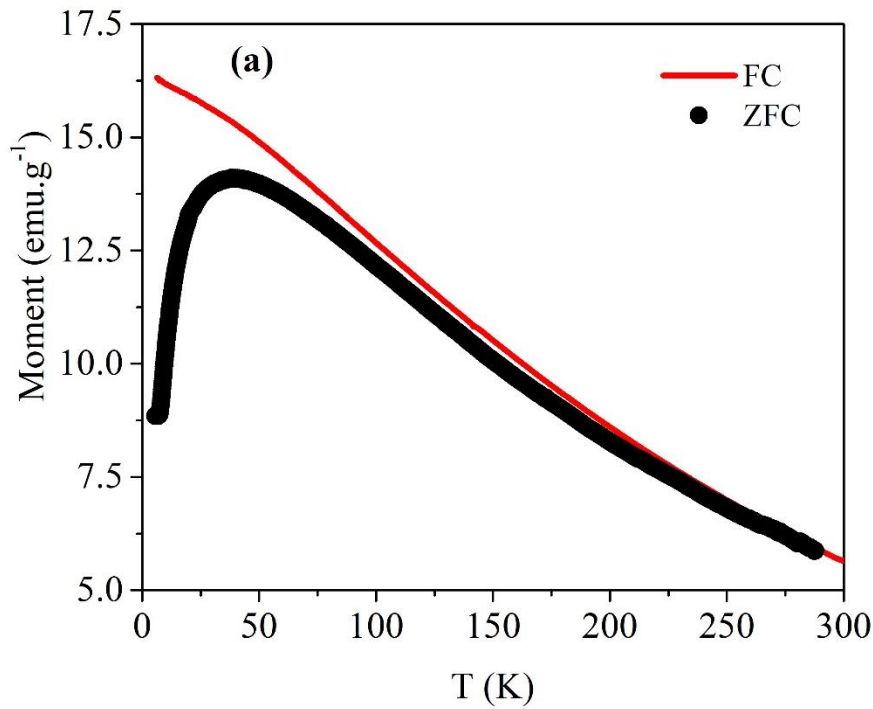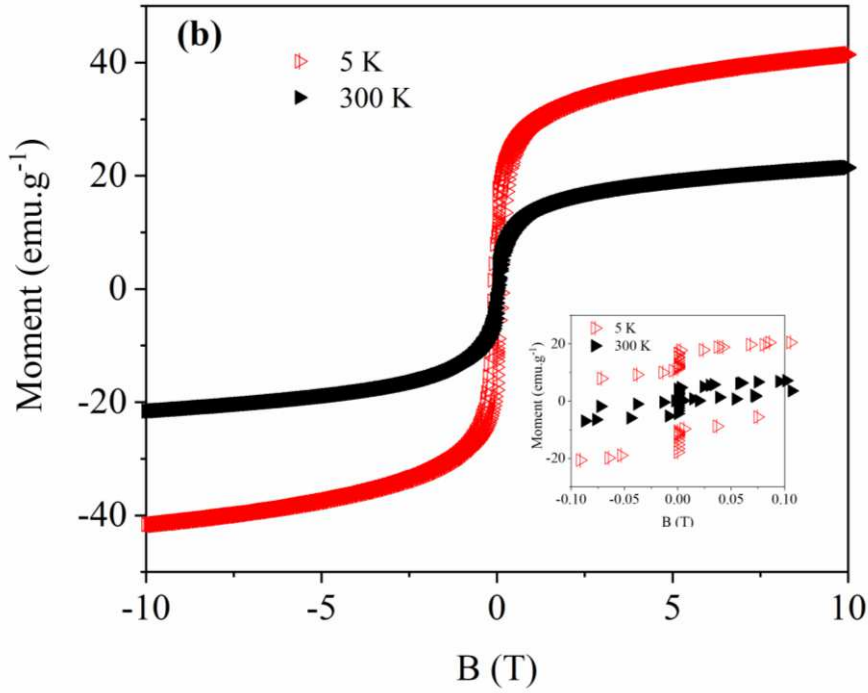
Figure 9.a) FC-ZFC curves and b) Hysteresis loops obtained at 5 and 300 K for 20MnFe/Si. The inset shows a close-up of the center of loops showing the neglected coercivity at room temperature.

To check that if an ideal noninteracting superparamagnetic picture can satisfactorily explain the magnetic behavior of the present composition, we have carried out a comprehensive study. In fact, magnetic nanoparticles are considered to be in superparamagnetic regime if i) the corresponding anhysteretic curves mannerly can be fitted to a single Langevin function or a weighted sum of Langevin functions and ii) the scaling of M/Ms with the ratio $M_S(B/T)$ is observed [50].

For the 20MnFe/Si, the scaling of M/M_S with the ratio $M_S(B/T)$ is not observed, as seen in figure 10.a. Moreover, the Langevin function fitting to the experimental curve deviates, according to figure 10.b.
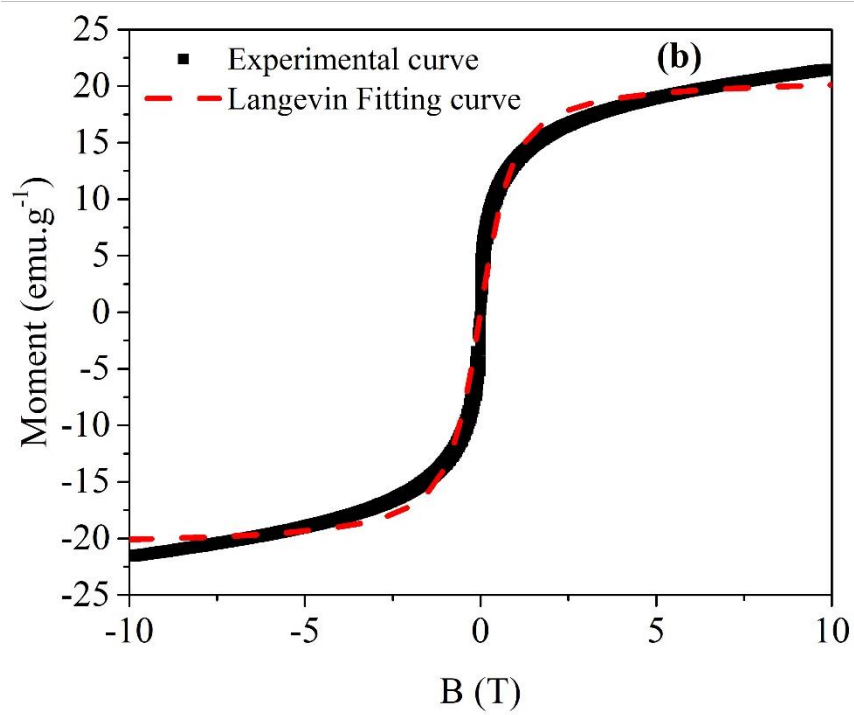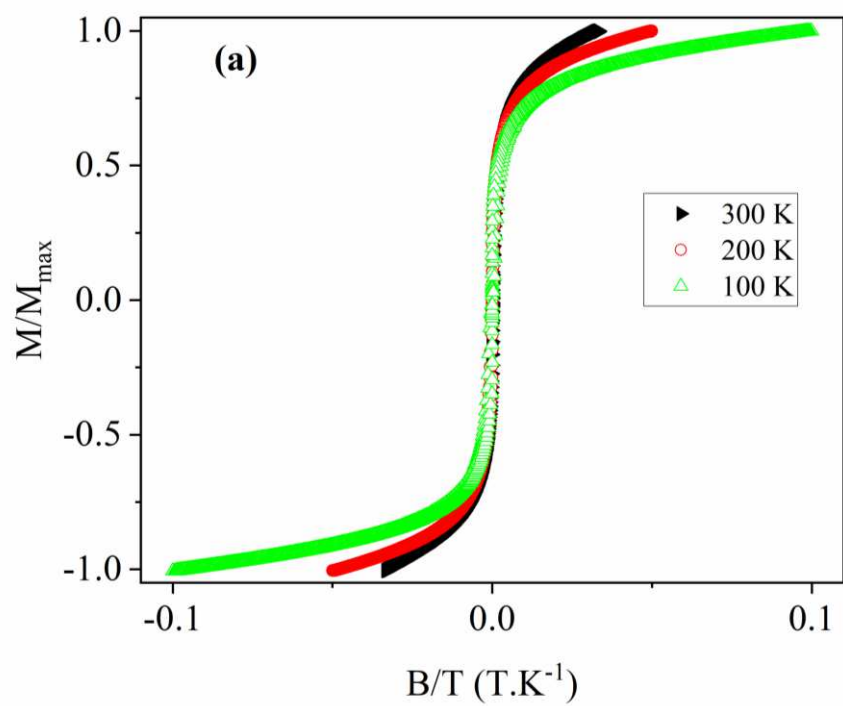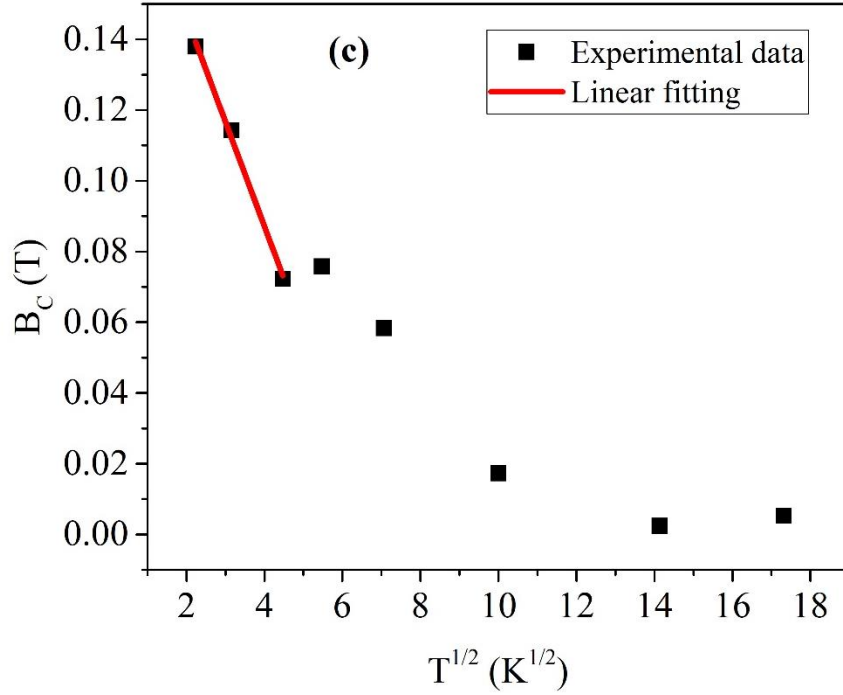
Figure 10.a) scaling plots, M/Mmax vs B/T, obtained at several temperatures above the blocking temperature, b) an unsuccessful attempt to fit the experimental hysteresis curve at room temperature to the Langevin equation and c) The coercive field vs. $T^{1/2}$ plot in accordance with eq. 7. The theoretical model only can adjust to the experimental data for temperatures below 30 K.

Therefore, the long-range and exchange interactions between isolated magnetic moments are effective and should be considered. This shows that the ideal noninteracting superparamagnetic model cannot be matched with the magnetic behavior of 20MnFe/Si and the magnetic interactions between the particles seem to be critical. The variation of coercivity as a function of temperature is given in figure 10.c. The coercivity was considered as the average value between negative and positive branches of the hysteresis loops. In accordance with Neel relaxation and the Bean-Livingston approaches, for an assembly of monodispersed and non-interacting magnetic nanoparticles, the temperature dependence of the coercivity as can be described as the following [51]:

$$B_C(T) = B_C(0)\left[1 - \left(\frac{T}{T_b}\right)^{\frac{1}{2}}\right],$$

$$B_C(0) \propto \frac{K_{eff}}{M_S}$$

where K_{eff} is the effective anisotropy constant. It is clear to see that such an approach is in agreement with experimental results only in temperatures below 30 K, T_b, where most of the particles are blocked. While above T_b, the theoretical model diverges from the experimental data. It can be argued that the behavior is related to the mixture of 2 different magnetic nanoparticle phases in a wide volume distribution with distinct anisotropy axes and relatively strong interparticle interactions [49].,

To support the VSM measurement, we performed a study using a local probe technique: ^{57}Fe Mössbauer spectrometry. The hyperfine structures obtained at 77 K and RT (as shown in figure 11) consist of a superposition of quadrupolar and magnetic components. At RT, the magnetic sextet with well-defined lorentzian lines can be clearly attributed to the presence of hematite (see the refined values given in Table 4). At 77K, the magnetic component, which shows asymmetrical and strongly broadened lines, has to be decomposed into two sub-components. The outer part that can be described by a single magnetic sextet with well-defined lines corresponds unambiguously to the presence of hematite (according to the refined values in Table 4). Moreover, it is important to note that (i) its proportions in terms of Fe content at 300 and 77K are quite similar and in good agreement with that estimated from X-ray patterns and (ii) the values of the quadrupolar shift at 300K and 77K suggest a poor crystallized form of hematite (defective structure, small crystalline domains, presence of Mn cations, role of silica matrix) [52]. The inner part of the magnetic component observed at 77K must be described by means of a distribution of hyperfine fields linearly correlated to that of the isomer shift. In addition, the quadrupolar components observed at 300K and 77K are best fitted by means of two quadrupolar doublets with two different values of isomer shift to describe the small asymmetry but their respective and accurate estimates remain difficult due to the lack of resolution of the central part : however, it can be concluded that they can be clearly attributed to Fe^{3+} species located in tetrahedral and octahedral sites of $MnFe_2O_4$ nanoparticles that show superparamagnetic relaxation phenomena. Such a feature is well consistent with the small size

(6-7 nm) as observed above by X-ray diffraction and TEM (see above). But the inner part of the magnetic component observed at 77K suggests clearly a distribution of size of the spinel ultrafine nanoparticles for which the superparamagnetic relaxation phenomena is fast.
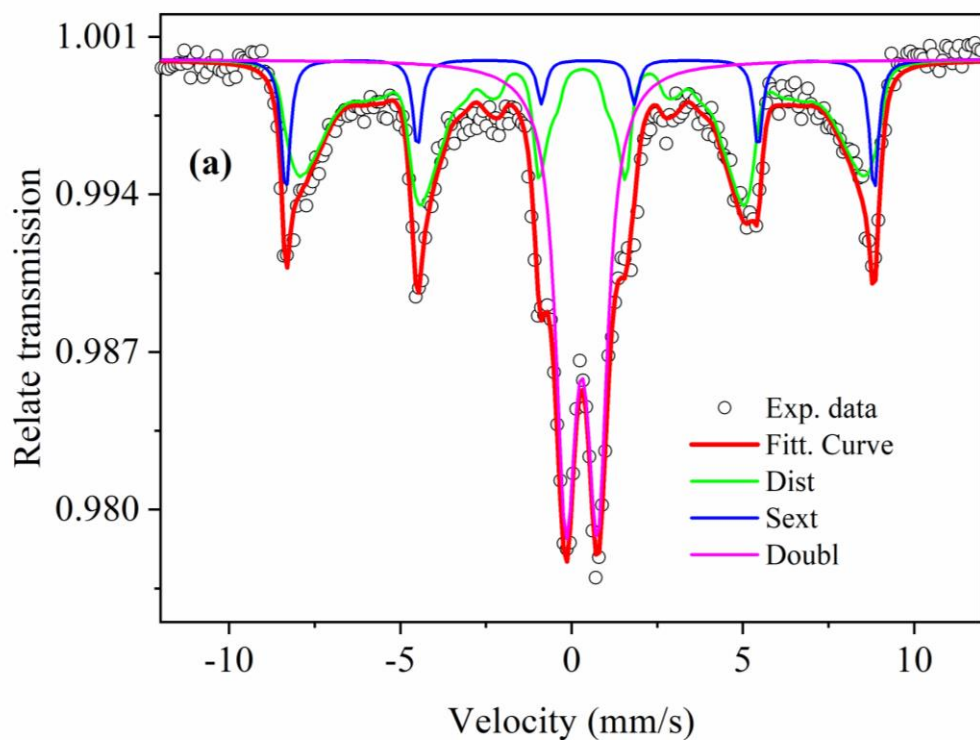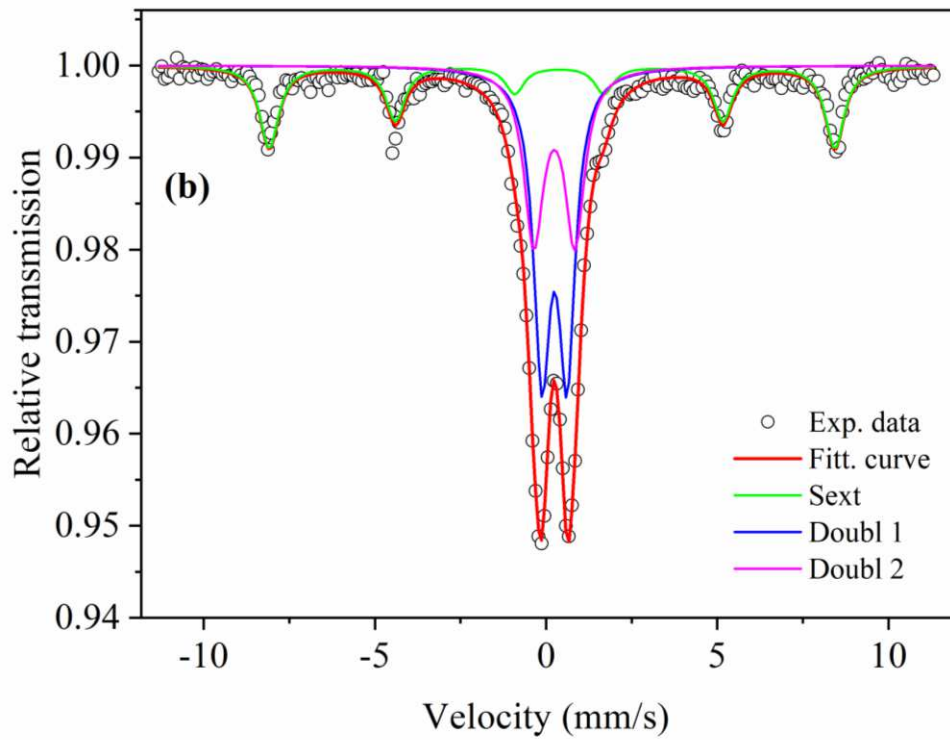
Figure 11 Mössbauer spectra measured at a) 77 K and b) RT.

Table 4) Refined values of hyperfine parameters obtained from fitting to room temperature and 77 K Mössbauer spectra of 20MnFe/Si (IS: Isomer shift; $\Delta/2\varepsilon$: Quadrupole splitting or quadrupole shift; B_{hf}: Hyperfine magnetic field; %: Area Percentage of each sub-spectrum). (Values fixed in the fitting procedure are given between right brackets; mean values obtained from fitting with distribution are given between <> brackets).

20MnFe/Si					
Temperature	IS (mm.s^{-1}) ± 0.01	$\Delta/2\varepsilon$ (mm.s^{-1}) ± 0.01	B_{hf} (T) ± 0.5	% ± 2	Site
300 K	0.39	-0.20	50.7	19	Hematite
	<0.35>	<0.91>	-	81	Spinel
77 K	0.50	-0.16	52.9	21	Hematite
	<0.46>	<0.01>	<40.1>	42	Spinel
	<0.45>	<0.95>	-	37	Smaller NPs Spinel

29

4) Conclusion

20MnFe/Si, was synthesized by a one-step auto-combustion route. XRD pattern confirmed the formation of $MnFe_2O_4$ with cubic spinel structure. However, the presence of a secondary phase of hematite was also confirmed. By means of the W-H method, the average size of $MnFe_2O_4$ nanocrystallites was found to be 6.5 nm. Moreover, the W-H analysis showed the compressive strain within the nanocomposite. Morphology of the nanocomposites was studied by TEM and confirmed the formation of spherical nanosized particles with a wide size distribution dispersed in amorphous silica.

A detailed study on dc electrical properties of 20MnFe/Si showed that the NNH model can represent a picture from the dc conduction mechanism in the sample. The impedance measurement revealed a non-Debye and thermally activated relaxation phenomena in 20MnFe/Si. Application of an equivalent circuit was considered to the complex impedance spectra of 20MnFe/Si assuming the grain and grain boundary contributions in conduction mechanism. A comprehensive investigation of the temperature dependence of the grain and grain boundary conductivity revealed a semiconducting-metallic-semiconducting transition over the temperature interval of 260 to 400 K. The transition is caused by a shift from the cation-anion-cation interaction to the cation-cation interaction occurring with the sample. By employment of the Jonscher power law to the ac conductivity of 20MnFe/Si, it was concluded that both OLPT and QMT models can explain the conduction nature over a whole measured temperature range, in agreement with the analysis given by the modulus and impedance studies.

Static magnetization measurements, VSM, were used to investigate the magnetic behavior of Mn-ferrite/silica nanocomposites. Despite the appearance of a relaxation peak at 33 K on ZFC curve characteristic of the superparamagnetic picture, the examination of the magnetization vs. magnetic field and the coercivity vs. temperature plots declared the magnetic behavior of 20MnFe/Si departs from the ideal non-interacting superparamagnetic picture. This behavior is suggested to be likely due to the particulate of small and big nanocrystallites with different magnetic anisotropy and the interparticle magnetic interactions taking place within the nanocomposite.

The room temperature and 77 K Mössbauer spectroscopy supported the VSM analysis. The Mössbauer spectrum displayed broad linewidth relaxed doublets and a magnetic sextet, this being related to the prominent superparamagnetic feature. The quantity of hematite

nanocrystalline in 20MnFe/Si was determined using the Mossbauer stuides being 20% . A good coherency was observed between the magnetic studies and the conduction mechanism explanations.

Conflict of Interests

The authors declare that they have no known competing financial interests or personal relationships that could have appeared to influence the work reported in this paper.

References

[1]   S. A. Salehizadeh, N. M. Ferreira, M. S. Ivanov, V. A. Khomchenko, J. A. Paixão, F. M. Costa, M. A. Valente, and M. P. F. Graça, Mater. Res. Bull. 131, 110972 (2020).

[2] Aakash, R. Choubey, D. Das, and S. Mukherjee, J. Alloys Compd. 668, 33 (2016).

[3] J. R. Huang and C. Cheng, J. Appl. Phys. 113, 33912 (2013).

[4] R.-R. Gao, Y. Zhang, W. Yu, R. Xiong, and J. Shi, J. Magn. Magn. Mater. 324, 2534 (2012).

[5] Z. Wang, Z. Li, Y. Zhang, R. Zhang, P. Qin, C. Chen, and L. Winnubst, Ceram. Int. 40, 4875 (2014).

[6] S. Güner, M. Amir, M. Geleri, M. Sertkol, and A. Baykal, Ceram. Int. 41, 10915 (2015).

[7] Z. Ž. Lazarević, Č. Jovalekić, A. Recnik, V. N. Ivanovski, M. Mitrić, M. J. Romčević, N. Paunović, B. D. Cekić, and N. Ž. Romčević, J. Alloys Compd. 509, 9977 (2011).

[8] K. Vamvakidis, M. Katsikini, D. Sakellari, E. C. Paloura, O. Kalogirou, and C. Dendrinou-Samara, Dalt. Trans. 43, 12754 (2014).

[9] M. Harada, M. Kuwa, R. Sato, T. Teranishi, M. Takahashi, and S. Maenosono, ACS Appl. Nano Mater. 3, 8389 (2020).

[10] M. A. Cobos, P. de la Presa, I. Llorente, J. M. Alonso, A. García-Escorial, P. Marín, A. Hernando, and J. A. Jiménez, J. Phys. Chem. C 123, 17472 (2019).

[11] M. Siddique and N. M. Butt, Phys. B Condens. Matter 405, 4211 (2010).

[12] L. I. Granone, A. C. Ulpe, L. Robben, S. Klimke, M. Jahns, F. Renz, T. M. Gesing, T. Bredow, R. Dillert, and D. W. Bahnemann, Phys. Chem. Chem. Phys. 20, 28267 (2018).

[13] D. K. Pradhan, S. Kumari, V. S. Puli, P. T. Das, D. K. Pradhan, A. Kumar, J. F. Scott, and R. S. Katiyar, Phys. Chem. Chem. Phys. 19, 210 (2017).

[14] A. Baykal, S. Esir, A. Demir, and S. Güner, Ceram. Int. 41, 231 (2015).

[15] S. A. Salehizadeh, M. P. F. Graça, and M. A. Valente, Phys. Status Solidi Curr. Top. Solid State Phys. 11, (2014).

[16] S. Baraghani, Z. Barani, Y. Ghafouri, A. Mohammadzadeh, T. T. Salguero, F. Kargar, and A. A. Balandin, ACS Nano acsnano.2c00378 (2022).

[17] Seema and S. Rohilla, AIP Conf. Proc. 2235, (2020).

[18] C. R. Vestal and Z. J. Zhang, Nano Lett. 3, 1739 (2003).

[19] C. Caparrós, M. Benelmekki, P. M. Martins, E. Xuriguera, C. J. R. Silva, L. M. Martinez, and S. Lanceros-Méndez, Mater. Chem. Phys. 135, 510 (2012).

[20] M. Nakhaei and D. S. Khoshnoud, J. Mater. Sci. Mater. Electron. 32, 14286 (2021).

[21] M. Stoia, C. Caizer, M. Ştefănescu, P. Barvinschi, and L. Barbu-Tudoran, J. Sol-Gel Sci. Technol. 58, 126 (2011).

[22] S. A. Salehizadeh, B. F. O. Costa, P. Sanguino, V. H. Rodrigues, J-M. Greneche, A. Cavaleiro, and M.A. Valente, Mater. Sci. Eng. B. under review (2022).

[23] R. Zamiri, H. Mahmoudi Chenari, H. F. Moafi, M. Shabani, S. A. Salehizadeh, A. Rebelo, J. S. Kumar, M. P. F. Graça, M. J. Soares, and J. M. F. Ferreira, Ceram. Int. 42, 12860 (2016).

[24] S. A. Salehizadeh, B. M. G. Melo, F. N. A. Freire, M. A. Valente, and M. P. F. Graça, J. Non. Cryst. Solids 443, 65 (2016).

[25] A. M. Jubb and H. C. Allen, ACS Appl. Mater. Interfaces 2, 2804 (2010).

[26] I. Chamritski and G. Burns, J. Phys. Chem. B 109, 4965 (2005).

[27] Y. Zhou, B. Xiao, S.-Q. Liu, Z. Meng, Z.-G. Chen, C.-Y. Zou, C.-B. Liu, F. Chen, and X. Zhou, Chem. Eng. J. 283, 266 (2016).

[28] M. A. G. Soler, T. F. O. Melo, S. W. Da Silva, E. C. D. Lima, A. C. M. Pimenta, V. K. Garg, A. C. Oliveira, and P. C. Morais, J. Magn. Magn. Mater. 272–276, 2357 (2004).

[29] P. Chandramohan, M. P. Srinivasan, S. Velmurugan, and S. V Narasimhan, J. Solid State Chem. 184, 89 (2011).

[30] D. Varshney, K. Verma, and A. Kumar, Mater. Chem. Phys. 131, 413 (2011).

[31] D. Souri, Z. E. Tahan, and S. A. Salehizadeh, Indian J. Phys. 90, 407 (2016).

[32] S. Balamurugan, M. D. Devi, I. Prakash, and S. Devaraj, Appl. Surf. Sci. 449, 542 (2018).

[33] J. M. D. Coey, Magnetism and Magnetic Materials (Cambridge University Press, Cambridge, 2010).

[34] H. Zheng, W. Weng, G. Han, and P. Du, J. Phys. Chem. C 117, 12966 (2013).

[35] Zamiri R, Salehizadeh SA, Ahangar HA, et al (2019) Dielectric and optical properties of Ni- and Fe-doped CeO_2 Nanoparticles. Appl Phys A Mater Sci Process 125:. https://doi.org/10.1007/S00339-019-2689-3

[36] K. Nadeem, F. Zeb, M. Azeem Abid, M. Mumtaz, and M. Anis Ur Rehman, J. Non. Cryst. Solids 400, 45 (2014).

[37] R. A. Lunt, A. J. Jackson, and A. Walsh, Chem. Phys. Lett. 586, 67 (2013).

[38] S. A. Saafan and S. T. Assar, J. Magn. Magn. Mater. 324, 2989 (2012).

[39] C. Behera, R. N. P. Choudhary, and P. R. Das, Ceram. Int. 41, 13042 (2015).

[40] P. Lunkenheimer, V. Bobnar, A. V Pronin, A. I. Ritus, A. A. Volkov, and A. Loidl, Phys. Rev. B 66, 52105 (2002).

[41] E. Veena Gopalan, K. A. Malini, S. Saravanan, D. Sakthi Kumar, Y. Yoshida, and M. R. Anantharaman, J. Phys. D. Appl. Phys. 41, 185005 (2008).

[42] J. Kolte, P. H. Salame, A. S. Daryapurkar, and P. Gopalan, AIP Adv. 5, 097164 (2015).

[43] S. A. Salehizadeh, H. M. Chenari, M. Shabani, H. A. Ahangar, R. Zamiri, A. Rebelo, J. S. Kumar, M. P. F. Graça, and J. M. F. Ferreira, RSC Adv. 8, 2100 (2018).

[44] M. Younas, M. Nadeem, M. Atif, and R. Grossinger, J. Appl. Phys. 109, (2011).

[45] J. B. Goodenough, Phys. Rev. 117, 1442 (1960).

[46] J. Jacob and M. A. Khadar, J. Appl. Phys. 107, 114310 (2010).

[47] E. Veena Gopalan, K. A. Malini, S. Saravanan, D. Sakthi Kumar, Y. Yoshida, and M. R. Anantharaman, J. Phys. D. Appl. Phys. 41, 185005 (2008).

[48] E. Oumezzine, S. Hcini, F. I. H. Rhouma, and M. Oumezzine, J. Alloys Compd. 726, 187 (2017).

[49] R. Zamiri, S. A. Salehizadeh, H. A. Ahangar, M. Shabani, A. Rebelo, J. Suresh Kumar, M. J. Soares, M. A. Valente, and J. M. F. Ferreira, Mater. Chem. Phys. 192, (2017).

[50] P. Tiberto, G. Barrera, F. Celegato, M. Coïsson, A. Chiolerio, P. Martino, P. Pandolfi, and P. Allia, Eur. Phys. J. B 86, 173 (2013).

[51] E. C. Mendonça, C. B. R. Jesus, W. S. D. Folly, C. T. Meneses, J. G. S. Duque, and A. A. Coelho, J. Appl. Phys. 111, 53917 (2012).

[52] R. E. Vandenberghe and E. De Grave, in Mössbauer Spectrosc., edited by Y. Yoshida and G. Langouche (Springer Berlin Heidelberg, Berlin, Heidelberg, 2013), pp. 91–185.

Supplementary Files

This is a list of supplementary files associated with this preprint. Click to download.

- GA.tif